



Wind effects on heat loss from a receiver with longitudinal tilt angle of small-scale linear Fresnel reflectors for urban applications

A. Barbón^a, C. López-Smeetz^c, L. Bayón^{b,*}, A. Pardellas^a

^a Department of Electrical Engineering, University of Oviedo, Spain

^b Department of Mathematics, University of Oviedo, Spain

^c Polytechnic School of Engineering of Gijón, University of Oviedo, Spain

ARTICLE INFO

Article history:

Received 1 June 2020

Received in revised form

5 October 2020

Accepted 8 October 2020

Available online 10 October 2020

Keywords:

Small-scale linear Fresnel reflector

Wind velocity

Wind direction

Heat losses

ABSTRACT

This paper presents an analysis of the wind effects, wind velocity and wind direction, on heat losses from a receiver with the longitudinal tilt angle of small-scale linear Fresnel reflectors for urban applications. In urban applications, the area required to install a solar collector is a critical parameter, therefore the parameter given by the energy-to-area ratio must reach its maximum value. Different combinations of longitudinal tilt angles are analyzed and compared with the typical configuration of a large scale linear Fresnel reflector (C1 configuration). The analysis is performed by SolidWorks Flow Simulation for different wind velocities and wind directions. Heat losses from the receiver have been estimated using a 3-D computational fluid dynamics model. Based on the numerical simulation of the receiver, the heat loss analysis has been calculated for several wind velocities, wind directions, and maximum energy-to-area ratio configurations. The effect of wind direction on heat losses is almost negligible. Although, heat losses are slightly higher in the North wind direction in most simulations. It will be demonstrated that the heat losses dramatically increase with a maximum energy-to-area ratio configuration, with the increase in longitudinal angle and, obviously, with the wind velocity. On the other hand, heat losses are higher at those locations with greater maximum energy-to-area ratio configuration. The heat losses, for wind velocity of 10 (m/s) and North direction, are, approximately, 120% of C1, 131% of C1, 143% of C1, 165% of C1 and 174% of C1, in Almeria, Rome, Budapest, Berlin and Helsinki, respectively. The longitudinal inclination of the receiver has positive effects on the performance of small scale linear Fresnel reflectors for urban applications.

© 2020 Elsevier Ltd. All rights reserved.

1. Introduction

Nowadays, our society faces significant challenges, such as: the transition to a low carbon energy system, the increase of pollution levels, and the high demand for energy. All these goals promote the search of an alternative and sustainable way to satisfy the energy demand and to reduce the pollution levels. Among other renewable energy sources, such as wind, geothermal or biomass, the solar energy meets two fundamental requirements: its abundant availability and its respect for the environment.

One of the great energy consumers in the European Union (EU) is the building sector. In particular, the final end use of energy in

building sector was about 27.2% in 2017 [1] with 9.48% and 17.72% for the commercial and residential sectors respectively. Heating and hot water both amount to 79% of the total final energy use in building sector whereas cooling is just a fairly small percentage in the total use [2].

Numerous studies conclude that for low and medium temperature applications, a small-scale linear Fresnel reflector (SSLFR) is suitable in building sector. For example, domestic water heating: [3–5], heating/cooling systems: [6–8], absorption of cooled air Solar-GAX cycle [9]; and absorption cooling system [10]. In addition, this collector can also be used in daylighting systems [11]. Some reasons for this suitability are: a simple design of its components, its high level of robustness, and its low manufacturing cost [12].

The basic geometry of a typical small-scale linear Fresnel reflector includes a primary reflector, a cavity receiver, and a receiver. Fig. 1 shows this geometry. The primary reflector is an

* Corresponding author.

E-mail addresses: barbon@uniovi.es (A. Barbón), UO231922@uniovi.es (C. López-Smeetz), bayon@uniovi.es (L. Bayón), apardellas@uniovi.es (A. Pardellas).

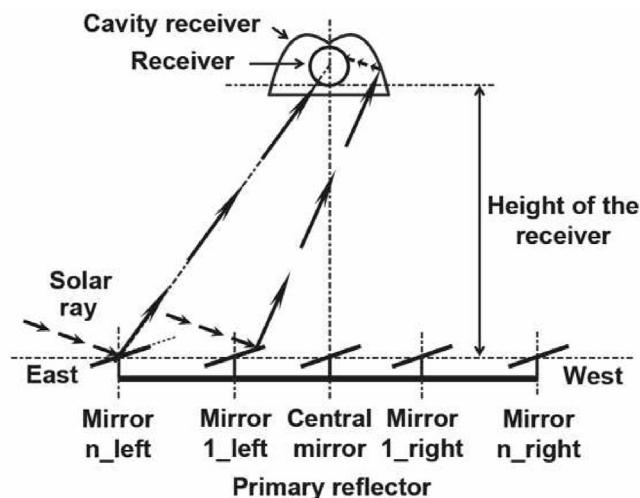


Fig. 1. Basic geometry of an SSLFR.

array of stretched mirrors which concentrate the sun's rays onto the receiver. As an SSLFR concentrates only the direct solar irradiance, a tracking system is needed to adjust the orientation of the mirrors according to the Sun position. For that purpose, the mirrors are equipped with single axis tracking to focus the solar irradiance onto the focal receiver. This movement is called elementary movement. The cavity receiver captures stray solar rays from the mirrors and reflects them onto the receiver. The receiver carries the working fluid. The receiver is placed at the middle of the SSLFR at the focal distance of the mirrors.

Different designs for the mirrors, the cavity receiver, and the receiver have been applied. The wide variety of existing designs in the literature indicates that there are not well-established designs that provide the optimal solutions [13]. In this study we will focus in the secondary reflector system. The first function of the cavity receiver is to minimize thermal losses by convection in the absorber tube, and the second one is to improve the optical performance of the SSLFR, reducing the number of off-target rays. A non-use of cavity receiver causes high optical losses [14] and high thermal losses. For that reason, several shapes of cavity receivers have been proposed: compound parabolic design [15], involute design [16], parabolic design [16], butterfly design [17,18], trapezoidal design [19], triangular design [20] and other complex geometries.

The conventional designs of the SSLFR have in common: (i) the mirrors and the receiver are parallel to the horizontal plane and (ii) the mirrors and the receiver are not provided with longitudinal movement. Some works found in the literature incorporate certain geometrical modifications designed to enhance their efficiency. Several authors, in addition to elementary movement, introduce other movements from different parts of the SSLFR: (i) Dai et al. [21] include both the East-West translation of the entire reflector field, according to the relative position of the Sun, and the rotation of a cavity receiver; (ii) Barbón et al. [22,23] include both the East-West axis rotation of the mirrors, and the East-West axis rotation of the receiver; (iii) Zhu et al. [24] include the axial axis rotation of the receiver. Other authors propose designs that allow the longitudinal inclination of the mirrors and/or the receiver [25,26]. None of these works take into account the effect of heat losses.

Several thermal models can be found in the literature, applied to lineal Fresnel reflectors: thermal resistance model and computational fluid dynamics model (CFD). The thermal resistance model is only applied to cross-section calculations. The computational fluid

dynamics model allows you to examine two or three dimensions.

Heimsath et al. [27] studied the temperature distribution and heat loss of a compound parabolic cavity. They used a thermal resistance model. This model incorporates the wind speed and wind direction. The model was developed for the two general receiver configurations: absorber tube surrounded by a glass envelope and receiver with a glass plate at the bottom. Montes et al. [15] proposed a thermal model of a compound parabolic cavity based on a thermal resistance model. The 2D model allows the study of the influence of the wind speed. Montes et al. [28] did a comparative analysis of the heat loss associated to three single-tube receiver designs with a compound parabolic cavity: evacuated, non-evacuated and non-evacuated with a glass plate at the aperture. They used a thermal resistance model. The analysis of the thermal loss for these three designs depended on the tube temperature and the wind velocity. In these works, the receiver is parallel to the horizontal plane.

Qiu et al. presented a double optical-thermal study of a compound parabolic cavity [29] and of a trapezoidal cavity [30]. In these works, the thermal performance was investigated by coupling the Monte Carlo ray tracing model with the finite volume method. The model incorporates the wind speed. In order to minimize the thermal heat losses of a trapezoidal cavity, Moghimi et al. [19] used CFD simulations. A 2D model has been simulated incorporating wind speed. They presented an accurate modeling of all the heat transfer mechanisms. The heat transfer rate and heat loss in a trapezoidal cavity are analyzed by Ref. [31]. They employed CFD model. In this work the number of tubes is evaluated changing the cavity angles while the downer edge of the trapezoidal cavity is constant. The model incorporates the wind speed. Moghimi et al. [32] presented the solution of the radiative transfer equation using a CFD model. They used a trapezoidal cavity. The 2D model incorporates the wind speed. They presented an accurate evaluation of cavity heat loss. In these works, the receiver is parallel to the horizontal plane.

A deep review on the relevant literature shows that the authors that investigated on the heat losses of receiver cavities, didn't deal with the longitudinal inclinations of the mirrors and/or the receiver.

The longitudinal inclination of the mirrors and/or the receiver shows positive effects in terms of energy absorbed by the receiver, and surface required for installation [26]. The available area, in urban applications, is one of the main limiting factors of the local energy production in buildings [33]. Therefore, this is a critical parameter. Barbón et al. [26] show how the longitudinal inclination of the mirrors and/or the receiver significantly reduces the required area for the SSLFR installation. But this study does not take into account heat losses due to the longitudinal inclination of the receiver.

In this paper the influence of wind on heat loss from a receiver with longitudinal tilt angle of small-scale linear Fresnel reflectors for urban applications is studied. This is its the original contribution. The analysis of the heat losses for various wind speeds and wind directions has been realized. The wind speeds we use are 1 (m/s), 2.5 (m/s), 5 (m/s), 10 (m/s) and 20 (m/s). The wind orientation goes from 0 to 180 ($^{\circ}$), in steps of 45 ($^{\circ}$). As longitudinal direction also influences our study, just because the computational fluid dynamics model (CFD) allows you to examine three dimensions, we have used the CFD method in this paper. In order to get this, the receiver has been modeled and analyzed using the CFD simulation. The validation of the model has been performed with the correlation presented by Montes et al. [28]. The 3-D numerical simulations have been carried out to investigate the heat losses from the receiver for different longitudinal inclinations, considering that the surface required for the installation of SSLFR is a

critical parameter.

The paper is organized as follows. In Section 2, basic constructive aspects of a small-scale linear Fresnel reflector and its heat losses are introduced. Section 3 presents a computational fluid dynamics model of the receiver: boundary conditions, material properties, mesh study and thermal model validation. Numerical simulations are presented in Section 4 for different wind velocities, wind directions, longitudinal angles, ambient temperatures, coating emissivities of the absorber tube and maximum energy-to-area ratio configurations. Finally, the conclusions are given in Section 5.

2. Modeling of an SSLFR

2.1. Constructive aspects of an SSLFR

Fig. 2 shows the systems that configure an SSLFR [12]. SSLFR incorporates parallel rows of stretched mirrors (7) (primary reflector system (3)) used for concentrating solar irradiance on the focal line of an absorber tube (secondary reflector system (4)). These parallel rows can form a longitudinal angle with the horizontal plane (β_M).

In this study, we are particularly interested in the secondary reflector system (see Fig. 3(a)). The secondary reflector system is mounted on a fixed structure, some meters above the primary reflector system, and contains the absorber tube (9), cavity receiver (10), isolation (11), glass covering (12), secondary structure (13), protective casing (14), and a secondary shaft (15). The secondary reflector system can form a longitudinal angle with the horizontal plane (β_a). The absorber tube (9) is encased in the receiver cavity (10) to reduce convective heat losses; for this purpose, the cavity receiver (10) is insulated and sealed with a glass cover (12) and silicon rubber beading. The absorber tube (9) is specially coated to increase its capability to absorb the incident solar irradiance. The absorber tube contains the working fluid. The absorber tube is a carbon steel tube, dull black painted. The cavity receiver consists of a polished stainless steel. Insulation consists of a glass wool. The glass covering is made of a tempered glass. The structure is made of a square hollow section of steel. The secondary reflector system is

covered with an aluminum sheet. The shaft is a galvanized steel tube. The secondary reflector geometry is presented in Fig. 3(b). Others systems of the SSLFR are the following: fixed structure (1), mobile structure (2), transmission systems (5) and tracking system (6).

2.2. Heat losses in a secondary reflector system with single-tube and glass-cover

Heat losses in the secondary reflector system (SRS) are produced by a complex mechanism that includes conduction heat transfer, convection heat transfer and radiation heat transfer. The study of heat losses is based on energy balances at each of the walls of the secondary reflector system (absorber tube, cavity receiver, insulation, casing, glass covering). Table 1 shows each wall used with its subscript (Sub.). Heat losses and its direction from the secondary reflector system are shown in Fig. 4 (see Table 2).

The secondary reflector system surfaces are continuously exposed to solar irradiance. The cavity receiver side walls absorb heat from the absorber tube surface by convection and radiation heat transfer. The cavity receiver side walls transfer heat to the glass cover by convection and radiation heat transfer, and to the inner casing surface by conduction through insulation. The absorption of direct solar irradiance by the casing is very little compared to the concentrated solar irradiance absorbed by the receiver [34].

Between the cavity receiver and the insulation there is an air gap. This fact is considered by several authors ([15,27]). For the same reason this study takes into account the air gap between the insulation and the casing. Glass cover gets heated up by convection and radiation heat transfer from the absorber tube, cavity receiver side walls, and by absorbing the incoming concentrated beam solar irradiance reflected by the rows of primary mirrors. The casing outer surfaces get heated up by conduction heat transfer from the cavity receiver inner surfaces through insulation and by absorption of beam solar irradiance and transfer heat to the ambient by convection and radiation heat transfer.

The Newton's Law of Cooling and the Stefan-Boltzmann Law are used to calculate convective exchange and the radiative exchange, respectively. Newton's Law of Cooling states that convection heat transfer is proportional to the difference between its own temperature and the ambient temperature:

$$q_{conv} = h_i \cdot A_i \cdot (T_i - T_{amb}) \tag{1}$$

where h_i is the heat transfer coefficient of the i th component wall of the secondary reflector system, A_i is the surface area of the i th component of the secondary reflector system, T_i is the surface temperature of the i th component wall of the secondary reflector system, and T_{amb} is the ambient temperature.

Stefan-Boltzmann Law states that radiation heat transfer is proportional to the difference between the fourth power of its own temperature and the fourth power of the ambient temperature.

$$q_{rad} = \sigma \cdot \epsilon_i \cdot A_i \cdot (T_i^4 - T_{amb}^4) \tag{2}$$

where σ is the Stefan-Boltzmann constant which is equal to $5.67 \cdot 10^{-8} (W/m^2K^4)$, ϵ_i is the emittance of the i th component wall of the secondary reflector system, A_i is the surface area of the i th component wall of the secondary reflector system, T_i is the surface temperature of the i th component wall of the secondary reflector system, and T_{amb} is the ambient temperature.

Several authors have calculated the heat flows shown in Fig. 4 [15,35–37]. The interaction of convective exchange and the radiative exchange makes extremely difficult to develop a purely

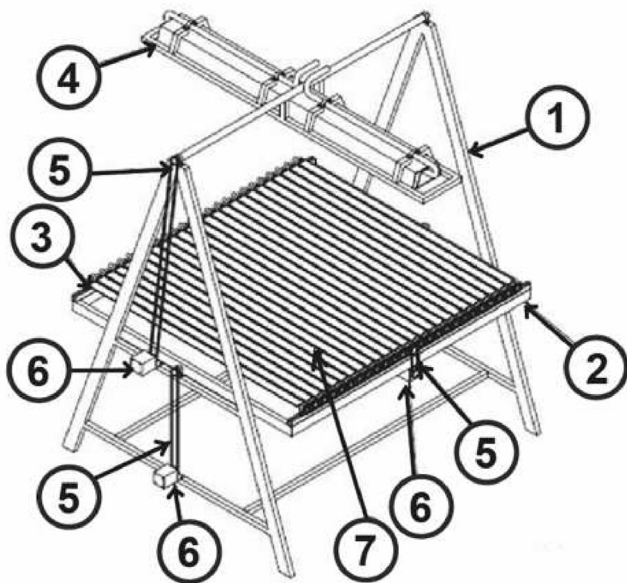


Fig. 2. Systems of an SSLFR.

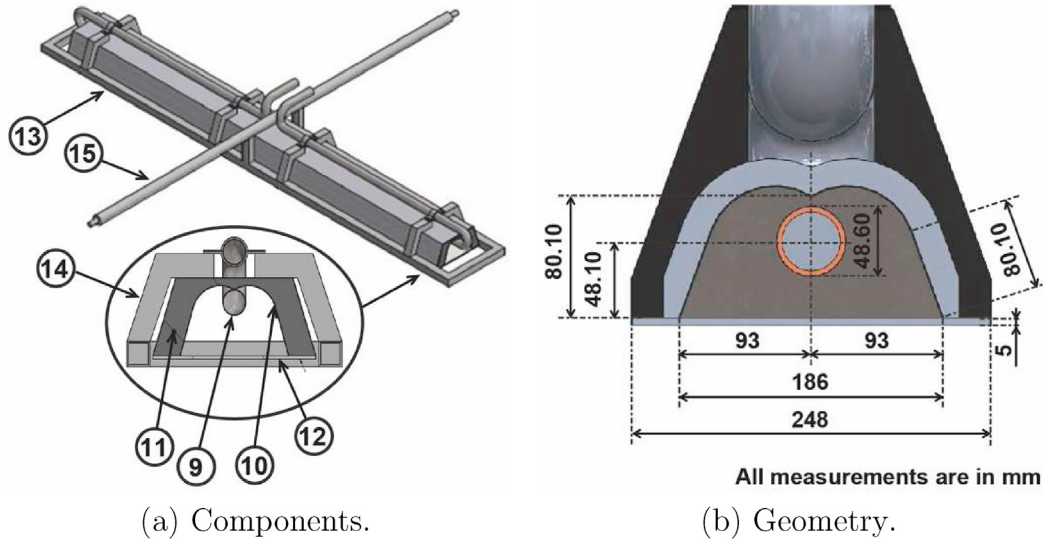


Fig. 3. Secondary reflector system.

analytical model for its estimation [38]. Therefore, several authors use computational fluid dynamics (CFD.) to calculate the heat losses in the absorber tube [31,32].

3. Computational fluid dynamics modeling

In general, computational fluid dynamics is a numerical technique in which equations describing the fluid flow are solved on a computer.

3.1. Flow and energy equations

The flow and heat transfer simulations in the secondary reflector system are carried out by solving continuity, momentum and energy equations simultaneously. The continuity, momentum and energy equations are given as [39]:

The continuity equation:

$$\nabla(\rho \vec{v}) = 0 \tag{3}$$

where ρ is the density, \vec{v} is the fluid velocity in the control volume, and $\nabla = \frac{\partial}{\partial x} + \frac{\partial}{\partial y} + \frac{\partial}{\partial z}$

The momentum equation:

$$\rho \vec{v} + \nabla \vec{v} = \vec{\nabla} p + \vec{\nabla} \cdot \vec{\tau} + \rho \vec{g} \tag{4}$$

where p is the static pressure, and $\vec{\tau}$ is the Reynolds stress tensor.

The energy equation:

$$\nabla \cdot (\rho c_p \vec{V} T) = \nabla \cdot (k \nabla T) \tag{5}$$

where c_p is the specific heat, and k is the thermal conductivity.

Eqs. (3)–(5) are extremely coupled and nonlinear, therefore, a numerical approximation approach has been carried out using a commercial computational fluid dynamics software. Thus, the governing equations have been solved using the finite volume method by segregated implicit solver. The secondary reflector system with single-tube and glass-cover has been designed in SolidWorks and it has been simulated in a CFD program, SolidWorks Flow Simulation [40]. This program is commonly used by several authors [36,41]. SolidWorks Flow Simulation [40] is a commercial computational fluid dynamics (CFD) solver based on the finite volume method. The numerical method used by Solidworks Flow Simulation is optimal for incompressible flows and flows with Mach Numbers less than 3.0. Temporal approximations of the continuity and convection/diffusion equations (for momentum, temperature, etc.) are used along with an operator splitting technique [42]. This technique is used to effectively solve the problem of pressure-velocity decoupling. Following an approach similar to SIMPLE [42], a discrete pressure equation of elliptical type is derived by algebraic transformations of the discrete equations originally derived for mass and momentum, taking into account the boundary conditions for velocity. This solver is extended by the broad set of physical models available for SolidWorks Flow Simulation like gravitation, radiation, real properties of various fluid media, etc. Radiation is a complex phenomenon and therefore there are a lot of simplified models of radiation. A Discrete Transfer model is used [42]. For the Ray Tracing model the heat radiations from solid surfaces, the emitted and the reflected one, both are assumed to be diffuse [42] (except for symmetry and mirror radiative surface types), i.e. they obey Lambert's law, according to which the radiation

Table 1
Subscripts that identify each wall of the SRS.

Sub.	Wall
0	Internal environment
1	Heat transfer fluid
2	Absorber tube (inner surface)
3	Absorber tube (outer surface)
4	Glass cover (inner surface)
5	Glass cover (outer surface)
6	Cavity receiver (inner surface)
7	Cavity receiver (outer surface)
Sub.	Wall
8	Air gap 1
9	Insulation (inner surface)
10	Insulation (outer surface)
11	Air gap 2
12	Casing (inner surface)
13	Casing (outer surface)
14	External environment

Table 2
Direction of the heat flow.

Heat flow	Heat transfer	From	To
$\dot{q}_{2 \rightarrow 1, conv}$	Convection	Absorber tube (inner surface)	Heat transfer fluid
$\dot{q}_{3 \rightarrow 2, cond}$	Conduction	Absorber tube (outer surface)	Absorber tube (inner surface)
$\dot{q}_{3 \rightarrow 0, conv}$	Convection	Absorber tube (outer surface)	Internal environment
$\dot{q}_{3 \rightarrow 0, rad}$	Radiation	Absorber tube (outer surface)	Internal environment
$\dot{q}_{0 \rightarrow 4, conv}$	Convection	Internal environment	Glass cover (inner surface)
$\dot{q}_{0 \rightarrow 6, conv}$	Convection	Internal environment	Cavity receiver (inner surface)
$\dot{q}_{0 \rightarrow 4, rad}$	Radiation	Internal environment	Glass cover (inner surface)
$\dot{q}_{0 \rightarrow 6, rad}$	Radiation	Internal environment	Cavity receiver (inner surface)
$\dot{q}_{4 \rightarrow 5, cond}$	Conduction	Glass cover (inner surface)	Glass cover (outer surface)
$\dot{q}_{5 \rightarrow 14, conv}$	Convection	Glass cover (outer surface)	External environment
$\dot{q}_{5 \rightarrow 14, rad}$	Radiation	Glass cover (outer surface)	External environment
$\dot{q}_{6 \rightarrow 7, cond}$	Conduction	Cavity receiver (inner surface)	Cavity receiver (outer surface)
$\dot{q}_{7 \rightarrow 8, conv}$	Convection	Cavity receiver (outer surface)	Air gap 1
$\dot{q}_{7 \rightarrow 8, rad}$	Radiation	Cavity receiver (outer surface)	Air gap 1
$\dot{q}_{8 \rightarrow 9, conv}$	Convection	Air gap 1	Insulation (inner surface)
$\dot{q}_{8 \rightarrow 9, rad}$	Radiation	Air gap 1	Insulation (inner surface)
$\dot{q}_{9 \rightarrow 10, cond}$	Conduction	Insulation (inner surface)	Insulation (outer surface)
$\dot{q}_{10 \rightarrow 11, conv}$	Convection	Insulation (outer surface)	Air gap 2
$\dot{q}_{10 \rightarrow 11, rad}$	Radiation	Insulation (outer surface)	Air gap 2
$\dot{q}_{11 \rightarrow 12, conv}$	Convection	Air gap 2	Casing (inner surface)
$\dot{q}_{11 \rightarrow 12, rad}$	Radiation	Air gap 2	Casing (inner surface)
$\dot{q}_{12 \rightarrow 13, cond}$	Conduction	Casing (inner surface)	Casing (outer surface)
$\dot{q}_{13 \rightarrow 14, conv}$	Convection	Casing (outer surface)	External environment
$\dot{q}_{13 \rightarrow 14, rad}$	Radiation	Casing (outer surface)	External environment

intensity per unit area and per unit solid angle is the same in all directions. This simulation tool solves the governing equations (momentum, continuity, and energy equations) under turbulent flow conditions. The turbulence in the flow has been treated

using the turbulent kinetic energy (k) and the turbulence dissipation rate (ϵ) using a standard $k - \epsilon$ turbulence model. The selected $k - \epsilon$ turbulent model is an usual model employed for similar studies [43–45]. The absorber tube inlet flow is assumed

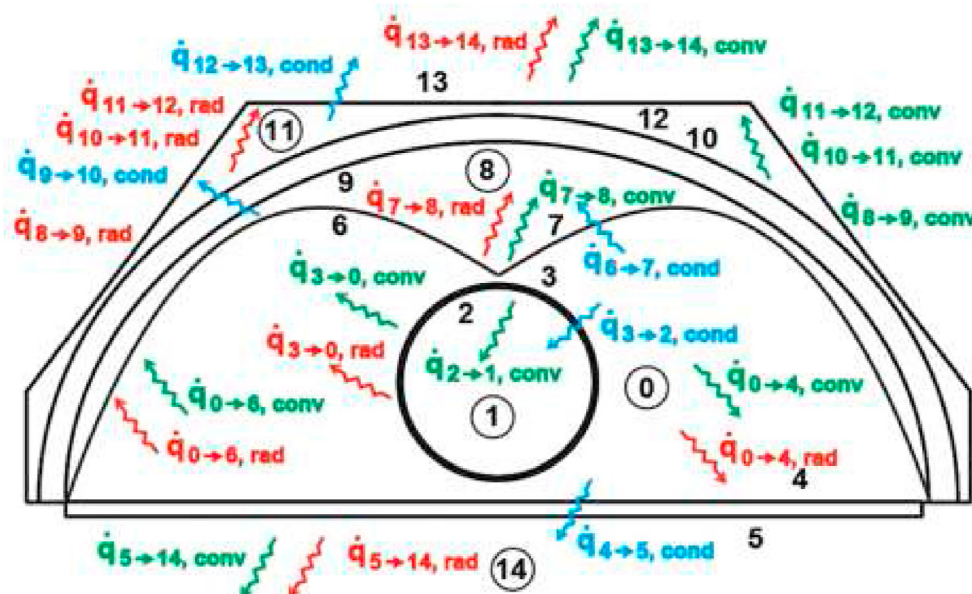


Fig. 4. Heat transfer between the different walls of the secondary reflector system.

to be fully developed.

3.2. Boundary conditions and material properties

Boundary conditions are the following:

- i) The ambient temperature is 20 (°C).
- ii) The atmospheric conditions with atmospheric pressure (1 (bar)).
- iii) Concentrated solar irradiance on the absorber tube is 2000 (W).
- iv) Inlet temperature of the working fluid is 100 (°C).
- v) Used wind speeds are 0 (m/s), 1 (m/s), 2.5 (m/s), 5 (m/s), 10 (m/s) and 20 (m/s).
- vi) Wind direction varies from 0 to 180 (°), in steps of 45 (°). Wind direction is generally reported in azimuth degrees, γ_w [46]. Wind direction is measured in degrees clockwise from the North. Therefore, a wind blowing from the North has a wind direction of 0 (°), and a wind blowing from the South has a wind direction of 180 (°).
- vii) Volumetric flow rate is 2600 (l/h).
- viii) It is considered that all the concentrated beam solar irradiance that reaches the aperture of the cavity are going to be directed on the absorber tube.
- ix) Absorption of direct solar irradiance by the casing is not considered in the analysis, as this absorption is significantly lower than the concentrated solar irradiance absorbed by the absorber tube [34].

The secondary reflector system is made of the following materials [12]: (i) The absorber tube is a carbon steel commercial tube 48.6 (mm) in outer diameter, 3.68 (mm) thick [47], and 2400 (mm)

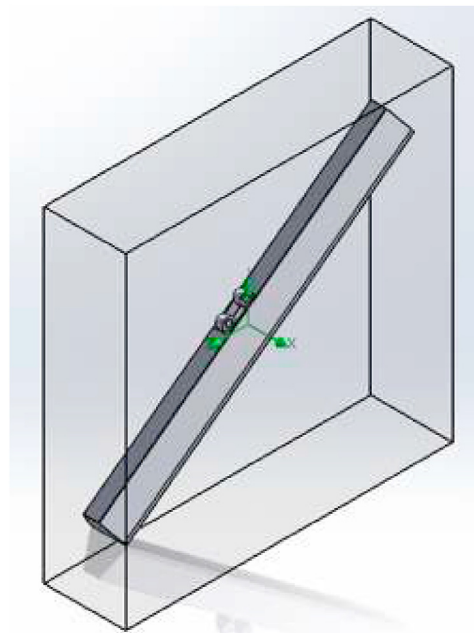


Fig. 5. Considered computational domain.

length; (ii) The cavity receiver consists of a polished stainless steel sheet 0.6 (mm) thick, and the aperture of the cavity receiver is 186 (mm) in width; (iii) The insulation consists of a glass wool filling 100 (mm) thick; (iv) The glass cover is made of a tempered glass 5 (mm) thick; (v) The structure is made of a steel square hollow section with dimensions 40x40x1.5 (mm); (vi) The secondary

Table 3
Material properties.

Component	Material	Density (kg/m ³)	Emissivity [51]
Working fluid	Oil [48]	$-0.7 \cdot T + 886$	-
Absorber tube	Carbon steel tube [39]	7833	0.49
Cavity receiver	Stainless steel 316 [39]	8000	0.1
Insulation	Glass wool [49]	70	0.1
Glass covering	Tempered glass [50]	2650	0.9
Casing	Aluminum sheet [39]	2787	0.9
Internal environment	Air [39]	$-0.0021 \cdot T + 1.2081$	-
Air gap 1	Air [39]	$-0.0021 \cdot T + 1.2081$	-
Air gap 2	Air [39]	$-0.0021 \cdot T + 1.2081$	-
External environment	Air [39]	$-0.0021 \cdot T + 1.2081$	-
Component	Density (kg/m ³)	Thermal conductivity (W/m ² °C)	
Working fluid	$-0.7 \cdot T + 886$	$-7 \cdot 10^{-5} \cdot T + 0.1342$	
Absorber tube	7833	$-0.034 \cdot T + 55.1$	
Cavity receiver	8000	$0.0121 \cdot T + 13.494$	
Insulation	70	0.034	
Glass covering	2650	1.5	
Casing	2787	$0.18 \cdot T + 164$	
Internal environment	$-0.0021 \cdot T + 1.2081$	$0.00007 \cdot T + 0.0245$	
Air gap 1	$-0.0021 \cdot T + 1.2081$	$0.00007 \cdot T + 0.0245$	
Air gap 2	$-0.0021 \cdot T + 1.2081$	$0.00007 \cdot T + 0.0245$	
External environment	$-0.0021 \cdot T + 1.2081$	$0.00007 \cdot T + 0.0245$	
Component	Specific heat (J/kg ² C)	Kinematic viscosity (m ² /s)	
Working fluid	$4.18 \cdot T + 1686.6$	$0.0031 \cdot T^{-1.398}$	
Absorber tube	465	-	
Cavity receiver	420	-	
Insulation	800	-	
Glass covering	786	-	
Casing	883	-	
Internal environment	$0.1364 \cdot T + 1001.2$	$8 \cdot 10^{-6} \cdot T^{0.2042}$	
Air gap 1	$0.1364 \cdot T + 1001.2$	$8 \cdot 10^{-6} \cdot T^{0.2042}$	
Air gap 2	$0.1364 \cdot T + 1001.2$	$8 \cdot 10^{-6} \cdot T^{0.2042}$	
External environment	$0.1364 \cdot T + 1001.2$	$8 \cdot 10^{-6} \cdot T^{0.2042}$	

reflector system is covered with an aluminum sheet 0.6 (mm) thick.

The thermo-physical properties of the secondary reflector system are listed in Table 3. We have used the emissivity values used by Pye [51]. These values were used for similar studies [19,31,38].

As boundary conditions, a rectangular prism has been created around the secondary reflector system with dimensions 600x3000x3000 (mm) (See Fig. 5). These dimensions have been selected so as not to affect the development of outer natural convection and not to increase too much the simulation time.

3.3. Mesh study

The computational mesh has been created by the SolidWorks Flow Simulation [40]. The automatic mesh generation is based on the Marching Voxel method composed of hexahedral elements. Our model consists of a global mesh and a local mesh. In this model, a structured mesh with tetrahedral elements has been developed to achieve a higher accuracy and a faster convergence. A very fine mesh is generated near the outer and the inner surface of the absorber tube to capture the high velocity and temperature gradients. In the calculations of the initial model, the number of total cells is 472,657. With this value was not qualified to the aim of the research. Therefore, by increasing it to 853,272 cells, the heat transfer rate is changing. Whereas, increasing the number of cells to the values greater than 853,272 does not lead to significant change in the results. As in this paper the influence of wind on heat loss from a receiver with longitudinal tilt angle of small-scale linear Fresnel reflectors for urban applications is studied by comparing different SSLFR configurations, it is concluded that, the meshing network with the 853,272 cells is acceptable and adequate for this study. Some meshes are displayed in Fig. 6.

3.4. Thermal model validation

The correlation of Montes et al. [28] has been used to validate the present model. This correlation is used in large-scale LFRs, configuration C_1 , where the parallel rows of mirrors form a longitudinal angle of 0° with the horizontal plane ($\beta_M = 0^\circ$) and the secondary reflector system forms a longitudinal angle of 0° with the horizontal plane ($\beta_a = 0^\circ$). Montes et al. suggest the following relationship:

$$q_{loss} = (0.0212 \cdot v_w - 0.6049) \cdot (T_t - T_{amb}) + 0.0135 \cdot q_i + 0.0072 \cdot (T_t - T_{amb})^2 - 1.046 \cdot 10^{-6} \cdot q_i \cdot (T_t - T_{amb}) - 9.582 \cdot 10^{-8} \cdot q_i^2 \quad (6)$$

where q_{loss} is the heat loss per length of the absorber tube (W/m), v_w is the wind velocity (m/s), T_t is the tube wall temperature ($^\circ C$), T_{amb} is the ambient temperature ($^\circ C$), and q_i is the concentrated flow on the absorber tube per tube perimeter and length unit (W/m^2). The reasons for using this correlation are the following: (i) This correlation focuses on a secondary reflector system with single-tube and glass-cover; (ii) Heat losses from the secondary reflector system have been analyzed with the wind flow; (iii) The validation of the correlation has been carried out through the work presented by Montes et al. [15]; (iv) The results of Montes correlation have been compared to numerical results [52]; (v) The results of Montes correlation have been compared to empirical results [53]; (vi) Montes correlation has been used by several

authors [54,55].

Fig. 7 shows the heat losses for Montes model and the proposed thermal model, as a function of the wind velocity and wind direction. As shown in Fig. 7, heat losses obtained with both models are very similar for the wind velocities (1, 2.5, 5, and 10 (m/s)), for North and South wind direction. In North wind direction, a deviation of 2.8% – 6.1% is observed in the total heat losses as shown in Fig. 6. In South wind direction, a deviation of 3.1% – 5.2% is observed in the total heat losses as shown in Fig. 6. The present model is considered to be validated as these deviations are not greater than 6.5% [56] or 10% [34]. Therefore, the CFD model is used for the heat loss analyses. For a wind velocity of 20 (m/s), the discrepancy is significant, because the highest wind speed they had used to settle Montes correlation was 12 (m/s). In this case, the deviation is the 17.2% and 17.3% for North and South wind direction, respectively.

In this paper the influence of wind on heat loss from a receiver with longitudinal tilt angle of small-scale linear Fresnel reflectors for urban applications is studied by comparing different SSLFR configurations. Our model is not precise. Anyway, as it uses the same model to study all the different configurations, we consider this comparison to be valid.

In Fig. 8 some pictures which give the temperature and heat flow distribution over the geometry, are presented for a wind speed of 0 (m/s). The temperature contours in the cross-section of the secondary reflector system are shown in Fig. 8.a. The temperature contours in the lengthwise section of the secondary reflector system are shown in Fig. 8.b. The heat flow distribution in the working fluid is shown in Fig. 8.c. Flow fields of air are shown in Fig. 9.a and Fig. 9.b, cross-section and lengthwise section, respectively. These images are output from Solidworks Flow Simulation.

4. Results and discussion

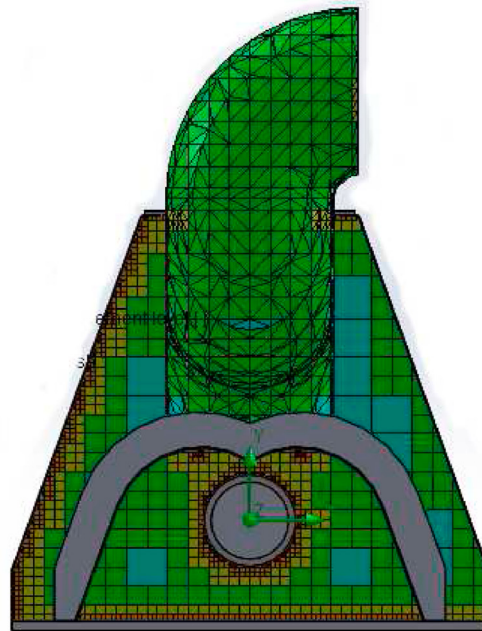
The aim of this section is to estimate the wind effects on heat losses from a secondary reflector system with longitudinal tilt angle (β_a) of small-scale linear Fresnel reflectors for urban applications. 3-D numerical simulations have been carried out for several geographic locations and compared with the configuration (C_1) used in large-scale LFRs. In C_1 configuration, the mirrors form a longitudinal angle of 0° with the horizontal plane ($\beta_M = 0^\circ$) and the absorber tube forms a longitudinal angle of 0° with the hori-

zontal plane ($\beta_a = 0^\circ$). It has been considered that SSLFR is perfectly aligned in a North-South orientation.

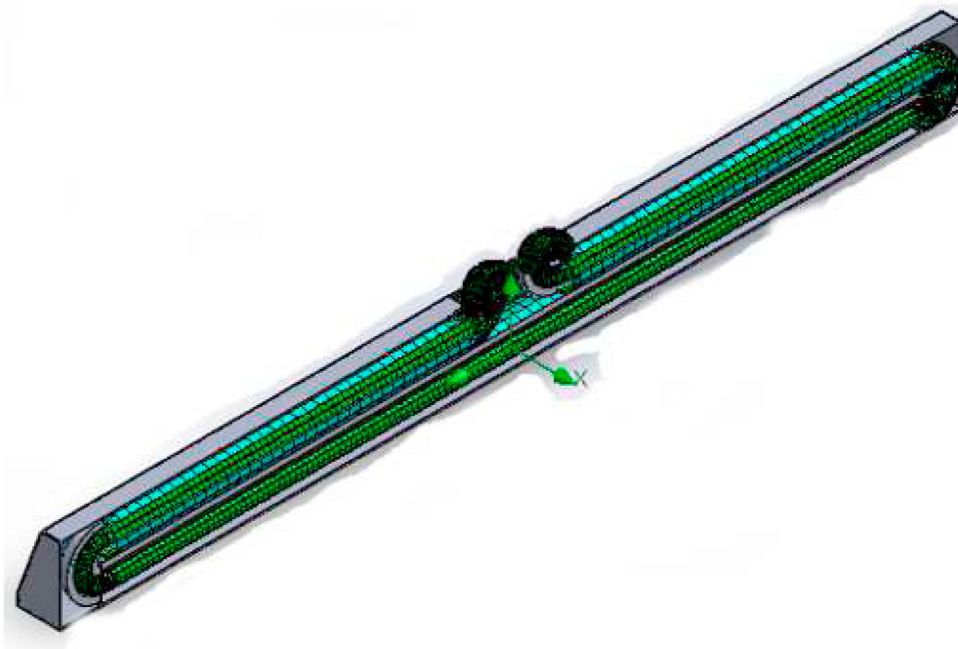
4.1. Case study

Table 4 shows the geographic characteristics of the cities under study.

We consider that the surface required for the installation of SSLFR is a critical parameter for urban applications. Thus, we will use the parameter energy-to-area ratio (EAR). This parameter, which is expressed in $MWh/m^2 ear$, is commonly used to compare SSLFR for urban applications [57]. The EAR is obtained by dividing the annual total energy absorbed by the absorber tube in Megawatt hours by area



(a) Mesh in the cross-section.



(b) Mesh in the lengthwise section.

Fig. 6. Mesh of the secondary reflector system.

required for the *SSLFR* installation in square meters. The *EAR* is expressed as follows:

$$EAR = \frac{E}{A} \tag{7}$$

The parameters of the *SSLFR* under analysis are listed in Table 5

[26]. These parameters remain constant in this study.

The maximum *EAR* results for the cities under study have been obtained in Ref. [26]. These results are shown in Table 6. These parameters remain constant in this study.

With the sign convention that we have adopted, lengths from the centre of the mirror to the left are considered positive, and

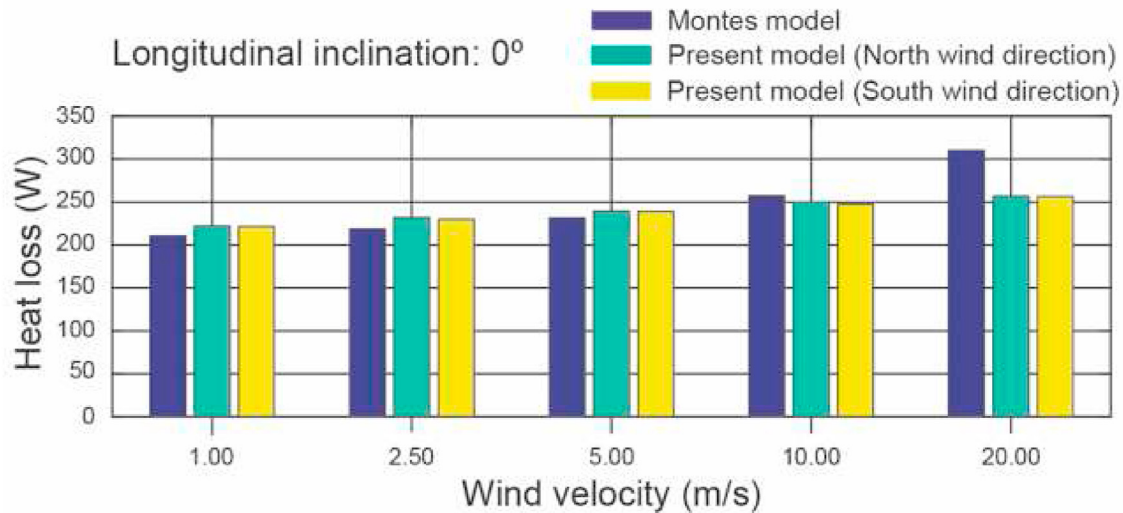


Fig. 7. Validation of the present model with the Montes model.

those to the right, negative. The following conclusions can be drawn from Table 6 for configuration of maximum EAR: (i) β_a equals the latitude of the geographic location; (ii) An increase in β_a increases L_a and therefore the exposed area; (iii) An increase in β_a increases the maximum EAR configuration.

4.2. Results and discussion

The heat losses in the secondary reflector system have been analyzed for various maximum EARs, various wind velocities, various wind direction, various longitudinal angles, various ambient temperatures, and various coating emissivities. The operating conditions considered for the heat losses analyses are the following: (i) A wind velocity range from 1 (m/s) to 20 (m/s); (ii) A wind direction range from 0 ($^\circ$) (North direction) to 180 ($^\circ$) (South) in steps of 45 ($^\circ$); (iii) The operating temperature of the working fluid is 100 ($^\circ$ C); (iv) The ambient temperature is 20 ($^\circ$ C); (v) The atmospheric pressure is 1 (bar); (vi) The concentrated solar irradiance on the absorber tube is 2000 (W); (vii) The volumetric flow rate is 2600 (l/h).

4.2.1. Effect of wind direction on secondary reflector system heat losses

The results of the simulations for maximum EAR are shown in Figs. 10 and 11 for the heat losses, wind directions, and wind velocities, in Almeria, and Helsinki, respectively. In Almeria, heat losses are similar for all wind directions. Although, heat losses are slightly higher in the North wind direction when the wind velocity increases. In Helsinki, heat losses are also similar for all wind directions. However, the North wind direction no longer prevails in all wind speeds. In order to simplify the presentation of results the North wind direction will be considered for the rest of the study.

4.2.2. Effect of longitudinal angle on secondary reflector system heat losses

The heat loss analyses have been carried out in Almeria by varying the longitudinal angle with a constant absorber tube length (2.4 (m)), a constant wind velocity (5 (m/s)), and maintaining North direction. The longitudinal angle has been varied from 12 ($^\circ$) to 36 ($^\circ$) in steps of 12 ($^\circ$). These heat losses are shown in Fig. 12. The heat

losses are directly proportional to the area exposed to the surroundings. The heat losses increase with an increase in the longitudinal angle due to a more heat transfer through the glass covering.

4.2.3. Effect of ambient temperature on secondary reflector system heat losses

The heat loss analyses have been carried out in Almeria by varying ambient temperature with a constant absorber tube length (2.4 (m)), a constant wind velocity (5 (m/s)), and maintaining North direction. The ambient temperature has been varied from 15 ($^\circ$ C) to 30 ($^\circ$ C) in steps of 2.5 ($^\circ$ C). These heat losses are shown in Fig. 13. The heat losses are directly proportional to the temperature difference between the surface and the surroundings, therefore the heat losses decrease with an increase in the ambient temperature.

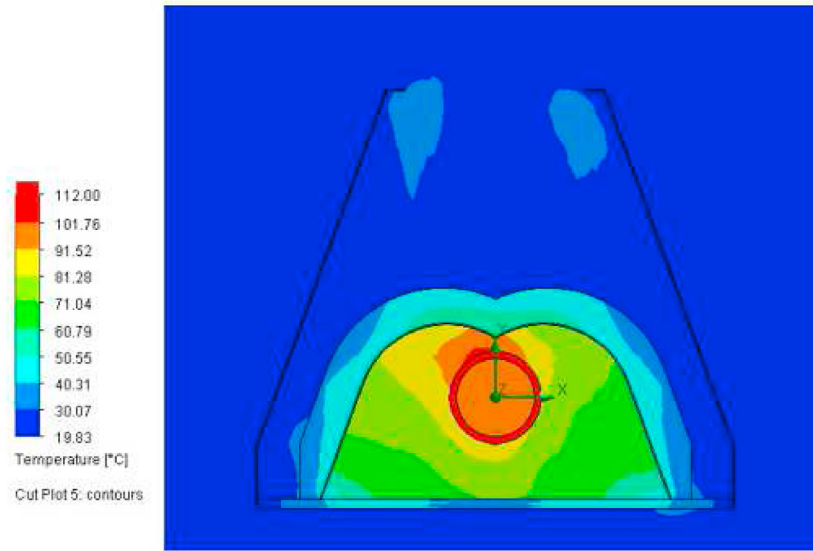
4.2.4. Effect of coating emissivity of the absorber tube on secondary reflector system heat losses

The heat loss analyses have been carried out in Almeria by varying the coating emissivity of the absorber tube with a constant absorber tube length (2.4 (m)), a constant wind velocity (5 (m/s)), and maintaining North direction. The coating emissivity of the absorber tube has been varied from 0.1 to 0.5 in steps of 0.1. These heat losses are shown in Fig. 14. The heat losses increase with an increase in the coating emissivity.

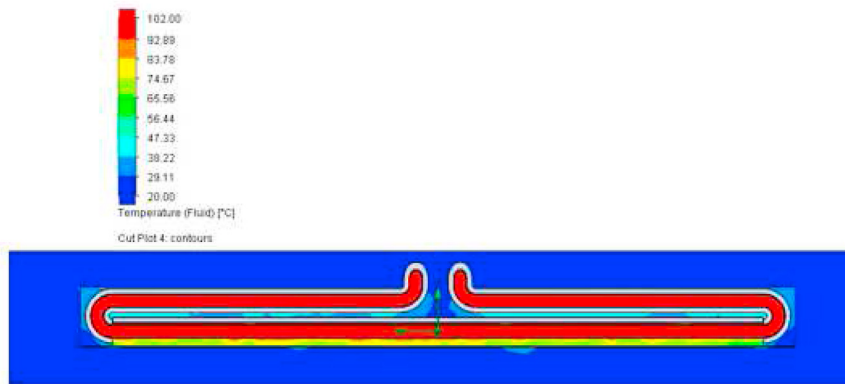
4.2.5. Effect of wind velocity on secondary reflector system heat losses

As it is shown in Table 6, the configuration C_1 has the same length of the absorber tube in all cities under study, therefore it also has the same exposed area. In contrast, the maximum EAR configuration has different length of the absorber tube, therefore it has different exposed area.

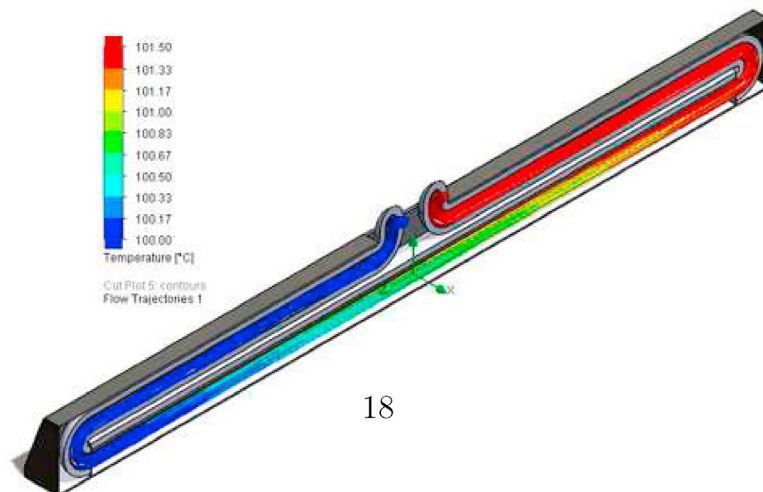
The heat loss analyses are carried out by varying wind velocity, and considering the North direction. These heat losses are shown in Fig. 15. It is obvious that heat losses increase as the wind velocity increases and maximum EAR configuration, because heat losses are directly proportional to the exposed area. As β_a equals the latitude of the geographic location and increasing β_a increases maximum EAR configuration, an



(a) Temperature contours in the cross-section.

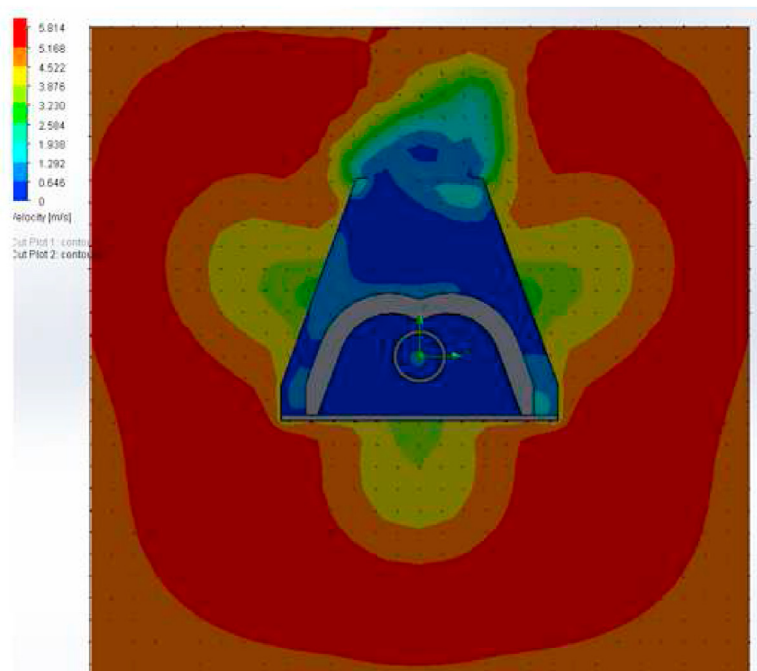


(b) Temperature contours in the lengthwise section.

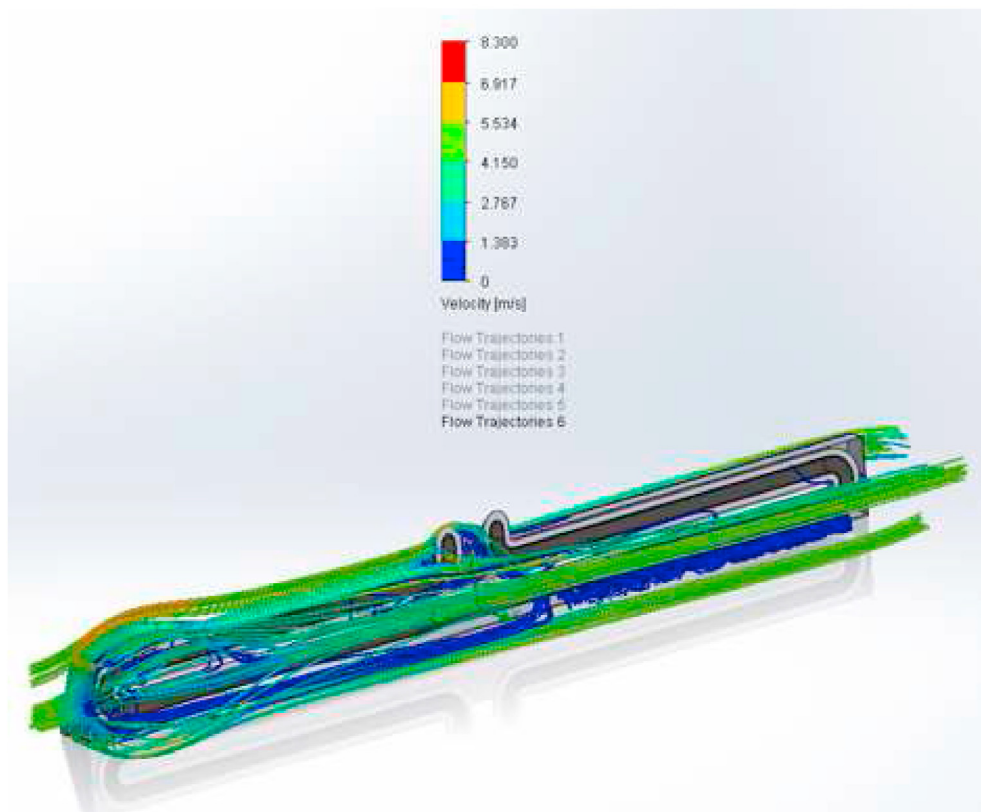


(c) Heat flow distribution in the working fluid.

Fig. 8. Temperature distribution in the SRS from Solidworks Flow Simulation.



(a) Cross-section.



(b) Lengthwise section.

Fig. 9. Flow fields of air.

Table 4
Cities under study [26].

Cities	Latitude	Longitude	Altitude
Almeria (Spain)	36°50'07" N	02°24'08" W	22 (m)
Rome (Italy)	41°53'30" N	12°30'40" E	52 (m)
Budapest (Hungary)	47°29'52" N	19°02'23" E	111 (m)
Berlin (Germany)	52°31'27" N	13°24'37" E	37 (m)
Helsinki (Finland)	60°10'10" N	24°56'07" E	26 (m)

increasing β_a also increases L_a and therefore the exposed area. The heat losses, for wind velocity of 10 (m/s), North direction, and maximum EAR configuration, are, approximately, 120% of C_1 , 131% of C_1 , 143% of C_1 , 165% of C_1 and 174% of C_1 , in Almeria, Rome, Budapest, Berlin and Helsinki, respectively. Therefore, the heat losses increase when the latitude of the geographic location increases, because β_a increases.

4.2.6. Effect of wind velocity on maximum EAR configuration

Fig. 16 shows the percentages with respect to configuration C_1 , of the maximum EAR, with and without heat losses for wind velocity 10 (m/s) and North wind direction, in Almeria, Rome, Budapest, Berlin and Helsinki, respectively. In this figure, the positive effects of the longitudinal inclination of the secondary reflector system without heat losses on the maximum EAR is noticeable [26]. When heat losses of the secondary reflector system are considered, the effect of the longitudinal inclination of the secondary reflector system on the maximum EAR decreases, but the effect remains positive with respect to configuration C_1 . Although heat losses are greater with the longitudinal inclination of the secondary reflector system, the total computing increases in EAR over the configuration C_1 . Therefore, it can be concluded that the longitudinal inclination of the secondary reflector system has positive effects on the design of SSLFR.

5. Conclusions

The objective of this work is to investigate the wind effects on heat losses from a receiver with longitudinal tilt angle of small-scale linear Fresnel reflectors (SSLFR) for urban applications at five European locations. As the area required for the SSLFR installation for urban applications is a critical parameter, the maximum energy-to-area ratio configurations have been used in this study.

Table 6
 C_1 and maximum EAR parameters [26].

Configuration C_1						
Cities	β_M (°)	β_a (°)	L_a^l (m)	L_a^r (m)	L_a (m)	
Almeria	0	0	- 0.037	- 2.037	2.00	
Rome	0	0	- 0.329	- 2.329	2.00	
Budapest	0	0	- 0.586	- 2.586	2.00	
Berlin	0	0	- 0.865	- 2.865	2.00	
Helsinki	0	0	- 1.343	- 3.343	2.00	
Configuration maximum EAR						
Cities	β_M (°)	β_a (°)	L_a^l (m)	L_a^r (m)	L_a (m)	Maximum EAR (% of C_1)
Almeria	18.418	36.836	1.236	- 1.098	2.334	142.54
Rome	20.946	41.892	1.262	- 1.238	2.500	179.60
Budapest	23.749	47.498	1.375	- 1.307	2.682	219.82
Berlin	26.260	52.520	1.502	- 1.392	2.894	272.30
Helsinki	30.085	60.169	1.784	- 1.512	3.296	412.76

The analysis has been performed with SolidWorks Flow Simulation for different wind velocities and wind directions. 3-D numerical simulations of heat losses in the secondary reflector system of an SSLFR have been carried out based on computational fluid dynamics (CFD) model. The correlation of Montes et al. [28] has been used to validate the CFD model. A good agreement between the simulated data and the correlation data was found for the wind velocities (1, 2.5, 5, and 10 (m/s)), because the deviations are not greater than 6.5%. For high wind velocities, correlation and simulated heat losses have a remarkable difference.

To evaluate the heat losses of the secondary reflector system, CFD simulations have been done. The heat losses in the secondary reflector system have been analyzed for different wind velocities, wind directions, maximum energy-to-area ratio configuration, longitudinal angles, ambient temperatures, and coating emissivities of the absorber tube. The heat losses are slightly higher in the North wind direction, in most simulations with increasing wind velocity. The heat losses increase with: the increase in the longitudinal angle, the decrease in the ambient temperature, and the increase in the coating emissivity of the absorber tube. The heat losses increase with wind velocity and maximum EAR configuration. The heat losses, for wind velocity of 10 (m/s) and North direction, are, approximately, 120% of C_1 , 131% of C_1 , 143% of C_1 , 165% of C_1 and 174% of C_1 , in Almeria, Rome, Budapest, Berlin and Helsinki, respectively. Therefore, the heat losses increase as the β_a increases.

Finally, an important conclusion was obtained: the positive effects of the longitudinal inclination of the secondary reflector

Table 5
Parameters of the SSLFR [26].

Parameters	Value
Number of mirrors at each side of the central mirror (n)	12
Mirror width (W_M)	0.060(m)
Separation between two consecutive mirrors (d)	0.024 (m)
Height of the receiver (f)	1.50 (m)
Outer diameter of the absorber tube (D)	0.0486 (m)
Mirror length (L_M)	2.00 (m)
Total length of the single absorber tube (L_a)	Depends of the city and maximum EAR
Left length of the single absorber tube (L_a^l)	Depends of the city and maximum EAR
Right length of the single absorber tube (L_a^r)	Depends of the city and maximum EAR
Reflectivity of the mirrors (ρ)	0.94 [58]
Cleanliness factors of the mirror (CL_m)	0.96 [59]
Cleanliness factors of the glass (CL_g) covering the secondary absorber	0.96 [59]
Transmissivity of this glass (τ)	$\tau = 0.87$ if $\alpha_i \leq 20^\circ$, $\tau = 0.85$ if $20^\circ \leq \alpha_i \leq 30^\circ$ [60]

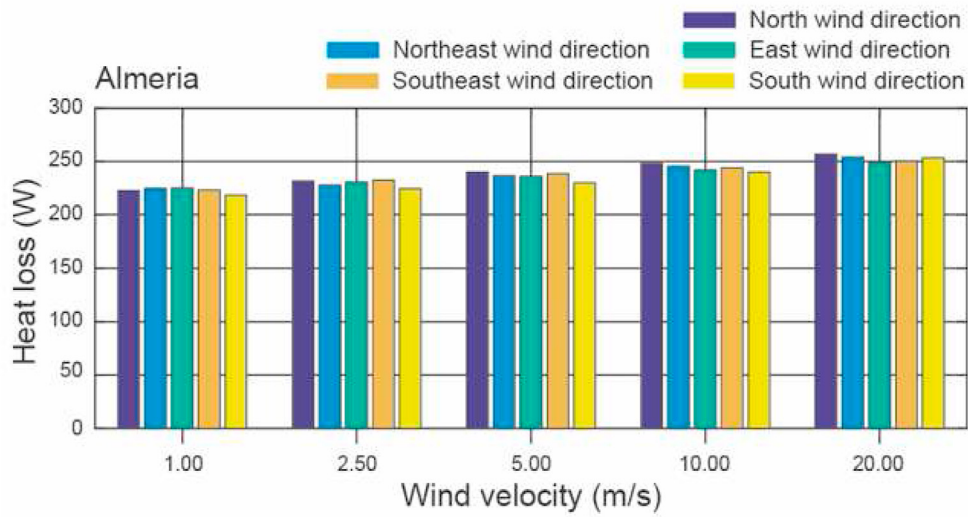


Fig. 10. Effect of wind direction on heat losses in Almeria.

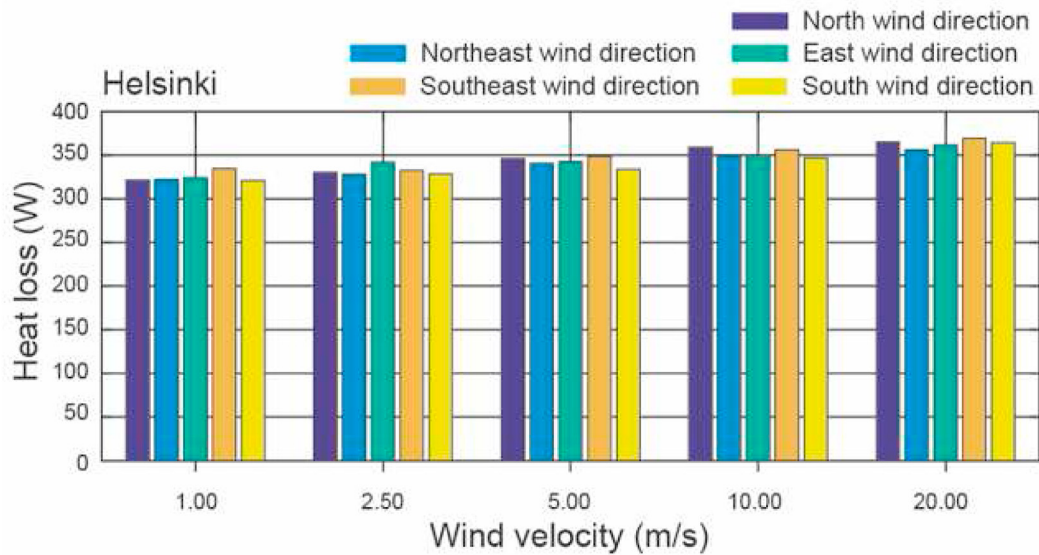


Fig. 11. Effect of wind direction on heat losses in Helsinki.

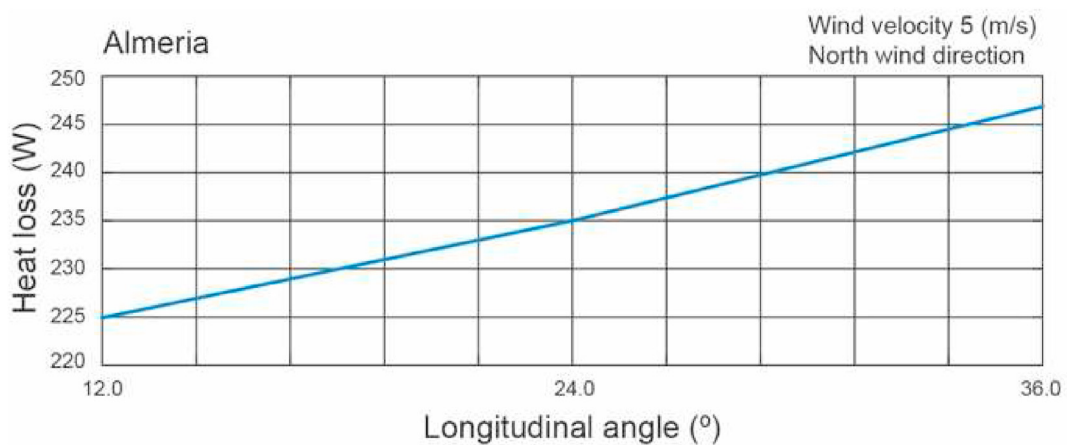


Fig. 12. Effect of longitudinal angle on heat losses in Almeria.

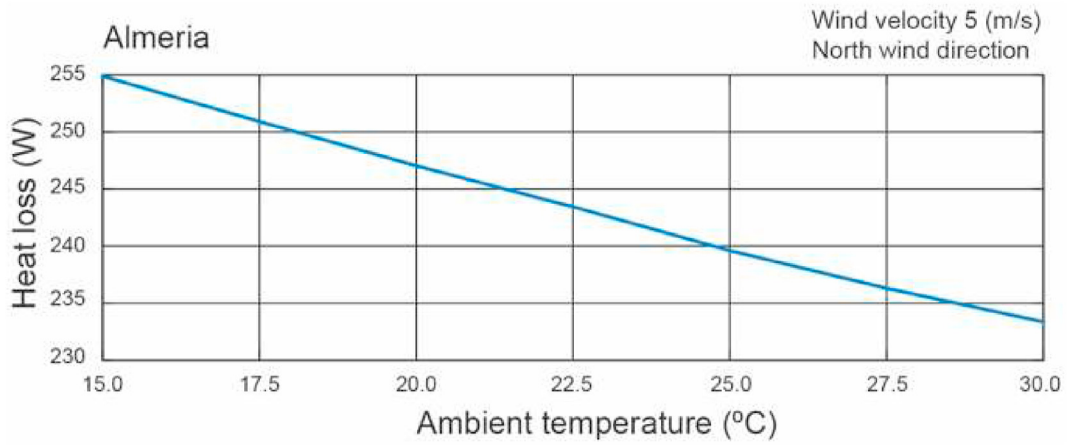


Fig. 13. Effect of ambient temperature on heat losses in Almeria.

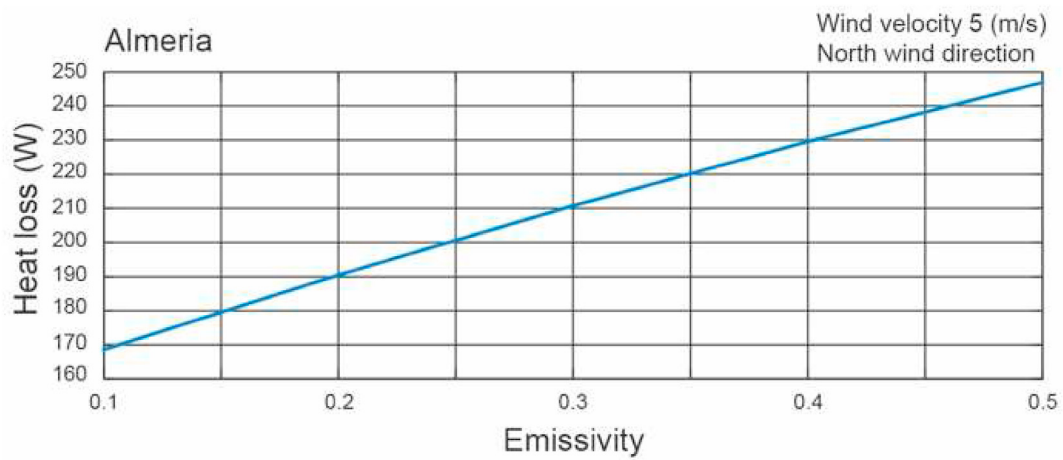


Fig. 14. Effect of coating emissivity on heat losses in Almeria.

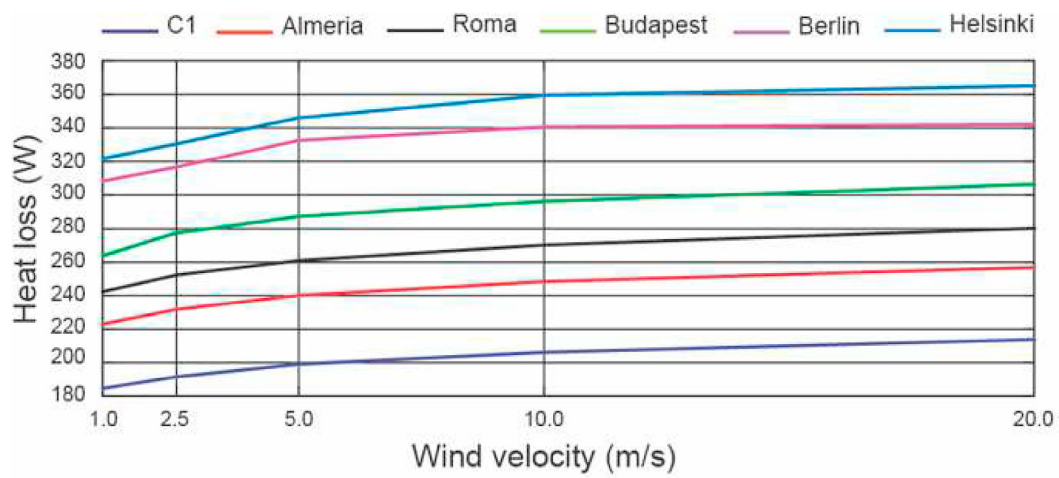


Fig. 15. Heat losses in C₁ and maximum EAR in the cities.

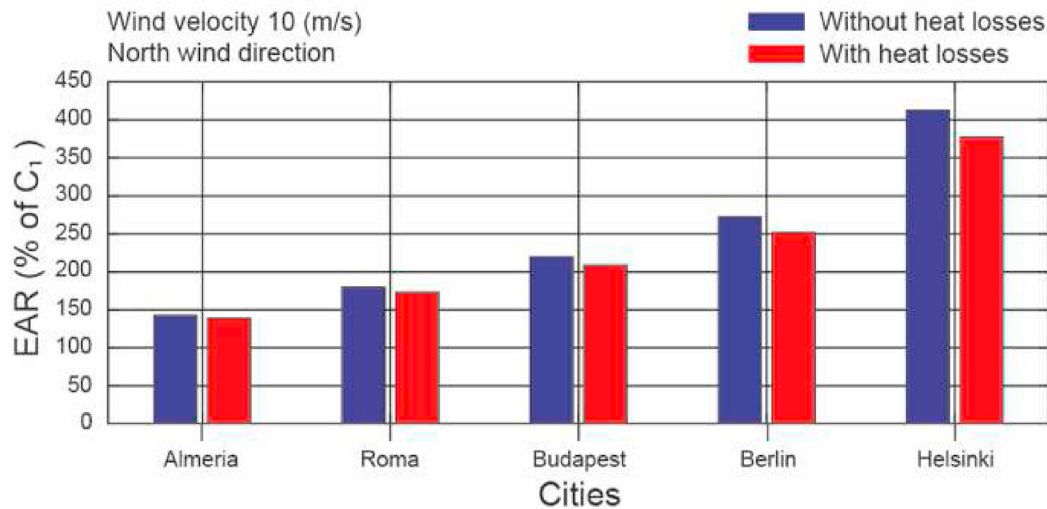


Fig. 16. Comparison maximum EAR, with and without heat losses.

system without heat losses on the maximum EAR which has already been demonstrated by other authors. When heat losses of the secondary reflector system are considered, the effect of the longitudinal inclination of the secondary reflector system on the maximum EAR decreases, but it remains positive with respect to configuration C_1 . Although, heat losses are greater with the longitudinal inclination of the secondary reflector system, the total computing increases in EAR with respect to configuration C_1 . Therefore, it can be concluded that the longitudinal inclination of the secondary reflector system has positive effects on the design of SSLFR.

Regarding perspectives of future, we consider that it would be interesting to carry out experimental works to validate the correlation of Montes.

CRedit authorship contribution statement

A. Barbón: Conceptualization, Methodology. **C. López-Smeetz:** Methodology, Data curation. **L. Bayón:** Software, Methodology. **A. Pardellas:** Software, Methodology, Writing - original draft.

Declaration of competing interest

The authors declare that they have no known competing financial interests or personal relationships that could have appeared to influence the work reported in this paper.

Acknowledgments

We wish to thank Dr. Laudino Rodríguez, head of the CIFP-Mantenimiento y Servicios a la Producción vocational training school in La Felguera, Asturias, Spain, for his work on the building of the prototype for the design presented in this paper.

References

- [1] EUROSTAT. Eurostat, Energy statistics -An overview. https://ec.europa.eu/eurostat/statistics-explained/index.php?title=Energy_statistics_-_an_overview#Energy_intensity, 2017. (Accessed 23 March 2020).
- [2] European Commission, Energy – heating and cooling, from, <https://ec.europa.eu/energy/en/topics/energyefficiency/heating-and-cooling>. (Accessed 23 March 2020).
- [3] T. Sultana, G.L. Morrison, G. Rosengarten, Thermal performance of a novel rooftop solar micro-concentrating collector, *Sol. Energy* 86 (2012) 1992–2000.
- [4] T. Sultana, G.L. Morrison, R.A. Taylor, G. Rosengarten, Numerical and experimental study of a solar micro concentrating collector, *Sol. Energy* 112 (2015) 20–29.
- [5] G. Mokhtar, B. Boussad, S. Noureddine, A linear Fresnel reflector as a solar system for heating water: theoretical and experimental study, *Case Stud. Therm. Eng.* 8 (2016) 176–186.
- [6] P. Bermejo, F.J. Pino, F. Rosa, Solar absorption cooling plant in Seville, *Sol. Energy* 84 (2010) 1503–1512.
- [7] F.J. Pino, R. Caro, F. Rosa, J. Guerra, Experimental validation of an optical and thermal model of a linear Fresnel collector system, *Appl. Therm. Eng.* 50 (2013) 1463–1471.
- [8] M.A. Serag-Eldin, Thermal design of a roof-mounted CLFR collection system for a desert absorption chiller, *Int. J. Sustain. Energy* 33 (2014) 506–524.
- [9] N. Velázquez, O. García-Valladares, D. Saucedo, R. Beltrán, Numerical simulation of a linear Fresnel reflector concentrator used as direct generator in a solar-GAX cycle, *Energy Convers. Manag.* 51 (2010) 434–445.
- [10] L. Zhou, X. Li, Y. Zhao, Y. Dai, Performance assessment of a single/double hybrid effect absorption cooling system driven by linear Fresnel solar collectors with latent thermal storage, *Sol. Energy* 151 (2017) 82–94.
- [11] A. Barbón, J.A. Sánchez-Rodríguez, L. Bayón, N. Barbón, Development of a fiber daylighting system based on a small-scale linear Fresnel reflector: theoretical elements, *Appl. Energy* 212 (2018) 733–745.
- [12] A. Barbón, J.A. Sánchez-Rodríguez, L. Bayón, C. Bayón-Cueli, Cost estimation relationships of a small scale linear Fresnel reflector, *Renew. Energy* 134 (2019) 1273–1284.
- [13] E. Bellos, C. Tzivanidis, A. Papadopoulos, Secondary concentrator optimization of a linear Fresnel reflector using Bezier polynomial parametrization, *Sol. Energy* 171 (2018) 716–727.
- [14] A. Barbón, C. Bayón-Cueli, L. Bayón, P. Fortuny Ayuso, Influence of solar tracking error on the performance of a small-scale linear Fresnel reflector, *Renew. Energy* 162 (2020) 43–54.
- [15] M.J. Montes, R. Barbero, R. Abbas, A. Rovira, Performance model and thermal comparison of different alternatives for the Fresnel single-tube receiver, *Appl. Therm. Eng.* 104 (2016) 162–175.
- [16] S. Balaji, K.S. Reddy, T. Sundararajan, Optical modelling and performance analysis of a solar LFR receiver system with parabolic and involute secondary reflectors, *Appl. Energy* 179 (2016) 1138–1151.
- [17] R. Grena, P. Tarquini, Solar linear Fresnel collector using molten nitrates as heat transfer fluid, *Energy* 36 (2011) 1048–1056.
- [18] M. Hack, G. Zhu, T. Wendelin, Evaluation and comparison of an adaptive method technique for improved performance of linear Fresnel secondary designs, *Appl. Energy* 208 (2017) 1441–1451.
- [19] M.A. Moghimi, K.J. Craig, J.P. Meyer, Optimization of a trapezoidal cavity absorber for the linear Fresnel reflector, *Sol. Energy* 119 (2015) 343–361.
- [20] F. Chen, M. Li, R.H. Emam Hassanien, X. Luo, Y. Hong, Z. Feng, M. Ji, P. Zhang, Study on the Optical Properties of Triangular Cavity Absorber for Parabolic Trough Solar Concentrator, *Hindawi Publishing Corporation International Journal of Photoenergy*, 2015. Article ID 895946, 9 pages.
- [21] J. Dai, H. Zheng, Y. Su, Z. Chang, The motional design and analysis for linear Fresnel reflector system combined three-movement, *Energy Procedia* 14 (2012) 971–976.
- [22] A. Barbón, N. Barbón, L. Bayón, J.A. Otero, Theoretical elements for the design of a small-scale linear Fresnel reflector: frontal and lateral views, *Sol. Energy* 132 (2016) 188–202.
- [23] A. Barbón, N. Barbón, L. Bayón, J.A. Otero, Optimization of the length and position of the absorber tube in small-scale Linear Fresnel Concentrators,

- Renew. Energy 99 (2016) 986–995.
- [24] Y. Zhu, J. Shi, Y. Li, L. Wang, Q. Huang, G. Xu, Design and experimental investigation of a stretched parabolic linear Fresnel reflector collecting system, *Energy Convers. Manag.* 126 (2016) 89–98.
- [25] A. Barbón, N. Barbón, L. Bayón, J.A. Sánchez-Rodríguez, Parametric study of the small-scale linear Fresnel reflector, *Renew. Energy* 116 (2018) 64–74.
- [26] A. Barbón, C. Bayón-Cueli, L. Bayón, L. Rodríguez, Investigating the influence of longitudinal tilt angles on the performance of small scale linear Fresnel reflectors for urban applications, *Renew. Energy* 143 (2019) 1581–1593.
- [27] A. Heimsath, F. Cuevas, A. Hofer, P. Nitz, W.J. Platzer, Linear Fresnel collector receiver: heat loss and temperatures, *Energy Procedia* 49 (2014) 386–397.
- [28] M.J. Montes, R. Abbas, M. Muñoz, J. Muñoz-Antón, J.M. Martínez-Val, Advances in the linear Fresnel single-tube receivers: hybrid loops with non-evacuated and evacuated receivers, *Energy Convers. Manag.* 149 (2017) 318–333.
- [29] Y. Qiu, Y.-L. He, Z.-D. Cheng, K. Wang, Study on optical and thermal performance of a linear Fresnel solar reflector using molten salt as HTF with MCRT and FVM methods, *Appl. Energy* 146 (2015) 162–173.
- [30] Y. Qiu, Y.-L. He, M. Wu, Z.-J. Zheng, A comprehensive model for optical and thermal characterization of a linear Fresnel solar reflector with a trapezoidal cavity receiver, *Renew. Energy* 97 (2016) 129–144.
- [31] S. Dabiri, E. Khodabandeh, A. Khoeini Poorfar, R. Mashayekhi, D. Toghraie, S.A. Abadian Zade, Parametric investigation of thermal characteristic in trapezoidal cavity receiver for a linear Fresnel solar collector concentrator, *Energy* 153 (2018) 17–26.
- [32] M.A. Moghimi, K.J. Craig, J.P. Meyer, A novel computational approach to combine the optical and thermal modelling of Linear Fresnel Collectors using the finite volume method, *Sol. Energy* 116 (2015) 407–427.
- [33] B. Giffith, P. Torcellini, N. Long, Assessment of the Technical Potential for Achieving Zero-Energy Commercial Buildings, ACEEE Summer Study Pacific Grove, 2006.
- [34] K.S. Reddy, K. Ravi Kumar, Estimation of convective and radiative heat losses from an inverted trapezoidal cavity receiver of solar linear Fresnel reflector system, *Int. J. Therm. Sci.* 80 (2014) 48–57.
- [35] E. Bellos, C. Tzivanidis, Alternative designs of parabolic trough solar collectors, *Prog. Energy Combust. Sci.* 71 (2019) 81–117.
- [36] C. Tzivanidis, E. Bellos, D. Korres, K.A. Antonopoulos, G. Mitsopoulos, Thermal and optical efficiency investigation of a parabolic trough collector, *Case Stud. Therm. Eng.* 6 (2015) 226–237.
- [37] S.A. Kalogirou, A detailed thermal model of a parabolic trough collector receiver, *Energy* 48 (2012) 298–306.
- [38] J. Fação, A.C. Oliveira, Numerical simulation of a trapezoidal cavity receiver for a linear Fresnel solar collector concentrator, *Renew. Energy* 36 (2011) 90–96.
- [39] J.H. Lienhard IV, J.H. Lienhard V, *A Heat Transfer Textbook*, third ed., Phlogiston Press, Cambridge, Massachusetts, 2003.
- [40] Solidworks, *Solidworks Flow Simulation 2018: Technical Reference*, Solidworks Corporation, Waltham, 2018.
- [41] E. Bellos, C. Tzivanidis, D. Tsimpoukis, Multi-criteria evaluation of parabolic trough collector with internally finned absorbers, *Applied, Energy* 205 (2017) 540–561.
- [42] https://www.solidworks.com/sw/docs/Flow_Basis_of_CAD_Embedded_CFD_Whitepaper.pdf, accessed on 24 August 2020.
- [43] P. Demissie Tegenaw, M. Gebreslasie Gebrehiwot, M. Vanierschot, On the comparison between computational fluid dynamics (CFD) and lumped capacitance modeling for the simulation of transient heat transfer in solar dryers, *Sol. Energy* 184 (2019) 417–425.
- [44] R. Zhang, P.A. Mirzaei, J. Carmeliet, Prediction of the surface temperature of building-integrated photovoltaics: development of a high accuracy correlation using computational fluid dynamics, *Sol. Energy* 147 (2017) 151–163.
- [45] A. Mwesigye, T. Bello-Ochende, J.P. Meyer, Heat transfer and thermodynamic performance of a parabolic trough receiver with centrally placed perforated plate inserts, *Appl. Energy* 136 (2014) 989–1003.
- [46] C. Zang, B. Gong, Z. Wang, Experimental and theoretical study of wind loads and mechanical performance analysis of heliostats, *Sol. Energy* 105 (2014) 48–57.
- [47] VEMACERO, <https://www.vemacero.com/Tablas/A53MP.pdf>, accessed on 21 August 2020.
- [48] REPSOL, https://www.repsol.com/imagenes/global/es/RP_MULTIGRADO_TERMICO_SINTETICO_tcm13-62589.pdf, accessed on 23 March 2020.
- [49] ISOVER, <https://www.isover.es/productos/acustilaine-70>, accessed on 23 March 2020.
- [50] N.P. Bansal, R.H. Doremus, *Handbook of Glass Properties*, first ed., Academic Press, Inc, London, 1986.
- [51] J.D. Pye, *System Modelling of the Compact Linear Fresnel Reflector*, PhD Thesis, University of New South Wales, Sydney, Australia, March 2008.
- [52] M. Mertins, *Technische und wirtschaftliche analyse von horizontalen Fresnel-kollektoren*, Ph.D. Thesis, University of Karlsruhe, Germany, 2009.
- [53] R. Barbero, A. Rovira, M.J. Montes, J.M. Martínez-Val, A new approach for the prediction of thermal efficiency in solar receivers, *Energy Convers. Manag.* 123 (2016) 498–511.
- [54] E. Bellos, C. Tzivanidis, A review of concentrating solar thermal collectors with and without nanofluids, *J. Therm. Anal. Calorim.* 135 (2019) 763–786.
- [55] K.S. Reddy, S. Balaji, T. Sundararajan, Estimation of heat losses due to wind effects from linear parabolic secondary reflector receiver of solar LFR module, *Energy* 150 (2018) 410–433.
- [56] S. Flores Larsen, M. Altamirano, A. Hernández, Heat loss of a trapezoidal cavity absorber for a linear Fresnel reflecting solar concentrator, *Renew. Energy* 39 (2012) 198–206.
- [57] A. Barbón, L. Bayón, C. Bayón-Cueli, N. Barbón, A study of the effect of the longitudinal movement on the performance of small scale linear Fresnel reflectors, *Renew. Energy* 138 (2019) 128–138.
- [58] J.A. Duffie, W.A. Beckman, *Solar Engineering of Thermal Processes*, fourth ed., John Wiley & Sons, New York, 2013.
- [59] V.M. Sharma, J.K. Nayak, S.B. Kedare, Effects of shading and blocking in linear Fresnel reflector field, *Sol. Energy* 113 (2015) 114–138.
- [60] P.H. Theunissen, W.A. Beckman, Solar transmittance characteristics of evacuated tubular collectors with diffuse back reflectors, *Sol. Energy* 35 (1985) 311–320.

Nomenclature

- CL_g : Cleanliness factor of the glass
 CL_m : Cleanliness factor of the mirror
 D : Diameter of the absorber tube (m)
 d : Separation between two consecutive mirrors (m)
 EAR : Energy-to-area ratio ($MWh/m^2/year$)
 f : Height of the receiver (m)
 L_a : Length of the single absorber tube (m)
 L_a^l : Left length of the single absorber tube (m)
 L_a^r : Right length of the single absorber tube (m)
 L_M : Length of the mirrors (m)
 n : Number of mirrors at each side of the central mirror
 q_{conv} : Convection heat transfer (W)
 q_i : Concentrated flux on the absorber tube per tube perimeter and unit length (W/m^2)
 q_{rad} : Radiation heat transfer (W)
 T_{amb} : Temperature ambient ($^{\circ}C$)
 T_t : Tube wall temperature ($^{\circ}C$)
 v_w : Wind velocity (m/s)
 W_M : Width of the mirrors (m)
 α_b : Absorptivity of the absorber tube
 β_a : Angle between the absorber tube and the horizontal plane ($^{\circ}$)
 β_M : Angle between the mirror axis and the horizontal plane ($^{\circ}$)
 P : Reflectivity of the primary mirrors
 T : Transmissivity of the glass